Wang *et al. Biochar* (2026) 8:84
https://doi.org/10.1007/s42773-026-00607-x

Biochar

ORIGINAL RESEARCH Open Access

Synergistic catalytic ozonation by pyridinic N and C=O groups on cotton hulls biochar for efficient DEET degradation

Chaozhong Wang[1,2,3], Yu Gao[2,3], Zhuang Guo[2,3], Xinyue Xie[2,3], Jian Wei[2,3], Zhiwei Song[1*] and Yonghui Song[2,3*]

Abstract

Based on the concept of resource utilization, this study successfully prepared a green and highly efficient nitrogen-doped biochar catalyst (N-BC-800) using agricultural waste cotton hulls as a raw material. This catalyst was then applied to the ozone-catalyzed degradation of N,N-diethyl-meta-toluamide (DEET), a typical insect repellent in water bodies. The apparent second-order rate constant reached 2358 M^{-1} s^{-1}, representing a 106-fold increase compared to the O_3 system alone, and a 25-fold increase compared to the O_3/BC system. Experimental characterization and theoretical analysis indicate that C=O groups and pyridinic N structures on the material surface serve as primary catalytic active sites. These synergistically promote ozone decomposition and generate highly reactive intermediates which are further converted into reactive oxygen species (ROS), significantly enhancing DEET degradation performance. This catalyst exhibits excellent stability and applicability in real aquatic environments. It demonstrates broad-spectrum degradation effects on multiple pollutants while significantly reducing the ecotoxicity of reaction byproducts. This study provides theoretical support and practical pathways for developing highly efficient, green ozone-catalyzed materials.

Highlights

- Agricultural waste is transformed into a highly effective water purification catalyst.
- Catalyst boosts ozone treatment efficiency by over 100-fold for pollutants.
- Surface active sites convert ozone into stronger reactive oxygen species.

Keywords Nitrogen-doped biochar, Ozone catalysis, Active sites, Resource utilization

*Correspondence:
Zhiwei Song
szwcyp@163.com
Yonghui Song
songyh@craes.org.cn
Full list of author information is available at the end of the article

Springer

Graphical Abstract

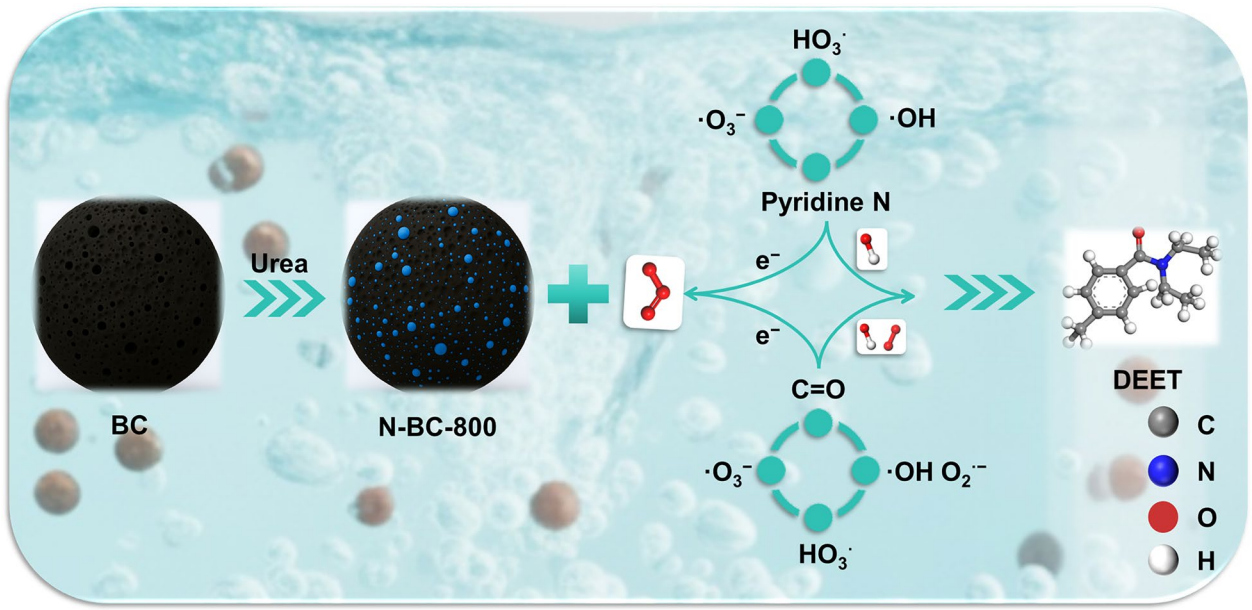

1 Introduction

N,N-diethyl-meta-toluamide (DEET) is a highly effective and broad-spectrum insect repellent used globally (Gao et al. 2020). Over 80% of DEET enters environment via domestic wastewater (Zhang et al. 2021). As a typical micropollutant, DEET concentrations in aquatic environments typically range from ng L^{-1} to μg L^{-1} levels. For instance, DEET has been detected in major Chinese rivers such as the Yangtze, Huai, Yellow, Hai, and Liao Rivers, with maximum concentrations reaching up to 10.2 ng L^{-1} (Liu et al. 2016). Owing to its environmental persistence and resistance to biodegradation, conventional wastewater treatment processes are often ineffective in its removal, leading to its widespread detection in aquatic systems at trace to micro levels (Liu et al. 2016). Studies indicate that DEET exhibits toxicity to aquatic organisms, such as green algae, and poses potential human health risks, including neurotoxicity, cardiotoxicity, and dermal irritation. To address the ecological and health risks brought by DEET, various treatment technologies have been applied to degrade persistent organic pollutants, such as adsorption, membrane separation, and advanced oxidation processes. Among them, heterogeneous catalytic ozonation technology has attracted much attention due to its simple operation, strong oxidation capacity and high mineralization efficiency (Fu et al. 2025).

This catalytic system utilizes solid catalysts to enhance the ozonation process, promoting the decomposition of ozone and generating ROS such as hydroxyl radicals. This mechanism not only facilitates the efficient breakdown of pollutants into less harmful by-products but also overcomes the limitations of traditional ozone processes, including high reaction selectivity and incomplete mineralization. In comparison, other catalytic systems such as photocatalysis, Fenton-like processes, and biological treatments have been explored for the removal of organic pollutants (Sun et al. 2019). Photocatalysis, for instance, achieves high degradation efficiency under UV light but is limited by its high energy consumption and reliance on specific light sources. The Fenton process, another widely used oxidation method, generates hydroxyl radicals for effective degradation. However, its application is often hindered by secondary pollutant formation and operational instability. While biological treatments are environmentally friendly, they are less effective for the treatment of high-concentration or toxic pollutants. In contrast, heterogeneous catalytic ozonation offers the advantage of operating efficiently without the need for external light or high chemical dosages, producing minimal secondary pollutants. Additionally, it provides

superior mineralization efficiency compared to some other catalytic systems, making it a promising technology for the treatment of persistent organic pollutants. However, The development of highly efficient ozone catalysts is crucial to optimizing this system's performance (Cheng et al. 2024).

Biochar, as a catalytic carrier, exhibits superior electron transfer efficiency and more diverse surface functional groups compared to traditional materials such as activated carbon and alumina, demonstrating significant advantages in the fields of green catalysis and environmental remediation. Its well-developed pore structure is conducive to the effective doping of active components, thus providing a good carrier foundation for the construction of high-performance catalysts. The raw materials for biochar are widely available, covering various biomass resources such as agricultural and forestry waste, livestock and poultry manure, algae and bacteria, sludge, and kitchen waste. However, the original biochar usually has a limited specific surface area, weak adsorption capacity, and insufficient active sites, which restricts the exertion of its catalytic performance (Wang et al. 2019a). For this reason, developing effective modification strategies to enhance its performance has become a research focus. Among them, heteroatom doping technology shows significant application potential by regulating the electronic structure of materials and increasing the number of active sites (Restivo et al. 2020).

Atomic doping, including both metal and non-metal elements, has proven effective in enhancing biochar catalysis (Fu et al. 2025). Metal doping (e.g., with Mn or Fe) can alter electron density, create new active sites, and introduce additional functional groups, thereby improving degradation efficiency (Tian et al. 2021). Nevertheless, metal leaching poses serious environmental and health risks, limiting large-scale application. Alternatively, non-metal doping has gained attention as a safer and more sustainable approach (Wang et al. 2016). Nitrogen-doped biochar (N-BC) incorporates N atoms into the carbon lattice, partially replacing carbon atoms and donating electrons to the sp^2-hybridized carbon matrix, which enhances catalytic performance. For instance, Cheng et al. (2024) demonstrated that nitrogen doping improved ozonation efficiency by nearly 50%. Recent studies also revealed that urea- and alkali-co-modified biochar achieves efficient peroxymonosulfate activation, where graphitic N and -COOH groups act as key active sites (Zhou et al. 2025). Despite these advances, the detailed catalytic mechanisms of N-BC in ozonation remain inadequately elucidated, necessitating further investigation.

In this study, agricultural waste cotton hulls and urea were used as raw materials to construct nitrogen-doped biochar with a high defect structure through two-step pyrolysis, which was used as an efficient and sustainable non-metallic catalyst for the effective removal of refractory organic pollutants in water bodies. The catalytic degradation performance of the material for DEET under various environmental conditions was systematically evaluated, and its applicability, stability, and reusability in different water quality matrices were investigated. By combining characterization methods such as XRD, XPS, FTIR, and EPR, the correlation mechanism between the material structure and performance was revealed. The broad-spectrum degradation capacity of the catalyst was further studied. This research provides a theoretical basis and technical approach for the high-value utilization of agricultural waste and the design of green advanced oxidation catalytic systems.

2 Materials and methods

2.1 Chemical reagents

The following reagents were purchased from Macklin (China) and used without further purification: urea, tert-butanol (TBA), methanol (MeOH), catalase (CAT), p-benzoquinone (BQ), trisodium phosphate anhydrous (Na_3PO_4), β-carotene, 5,5-dimethyl-1-pyrroline (DMPO), p-chlorobenzoic acid (pCBA), nitroblue tetrazolium chloride (NBT), ibuprofen (IBP), N,N-diethyl-m-toluamide (DEET), primidone (PRM), atrazine (ATZ), ketoprofen (KET), potassium indigo trisulfonate, monosodium phosphate (NaH_2PO_4), sodium sulfate anhydrous (Na_2SO_4), sodium bicarbonate ($NaHCO_3$), and sodium chloride (NaCl). All chemicals were of analytical grade. Natural organic matter (NOM) was sourced from the International Humic Substances Society (USA), and ultrapure water (18.2 MΩ) was employed in all experiments.

2.2 Synthesis of nitrogen-doped biochar

Biochar (BC) was prepared from cotton hulls, which were washed repeatedly with deionized water, dried, and then pyrolyzed in a tubular furnace under a nitrogen atmosphere (nitrogen flow rate: 0.15 L min^{-1}). The pyrolysis process was carried out at a heating rate of 5 °C min^{-1} up to 800 °C, followed by a 2-h holding time at the target temperature. The resulting product was collected after cooling and used as the raw BC. Nitrogen-doped biochar (N-BC) was synthesized by pyrolyzing a mixture of raw BC and urea. In a typical procedure, a certain mass of BC was thoroughly ground with urea (mass ratio of urea to BC = 0.25:1,0.5:1,1:1 and 1.5:1) for 30 min. The mixture was then heated in the tubular furnace under nitrogen (nitrogen flow rate: 0.15 L min^{-1}) at 5 °C min^{-1} to different target temperatures (600, 700, 800, and 900 °C) and maintained for

2 h. The resulting N-BC samples were collected after cooling. The obtained catalysts were labeled according to their pyrolysis temperature as N-BC-600, N-BC-700, N-BC-800, and N-BC-900.

2.3 Analytic characterization

The morphological and elemental features of the samples were examined by scanning electron microscopy (SEM, Thermo Scientific Apreo 2S) and transmission electron microscopy (TEM, Talos F200S). Physical and chemical properties were identified through X-ray diffraction (XRD, Bruker D8 ADVANCE), Fourier-transform infrared spectroscopy (FTIR, Bruker Tensor 27), Raman spectroscopy (Horiba Scientific LabRAM HR Evolution), X-ray photoelectron spectroscopy (XPS, Thermo Fisher ESCALAB 250Xi), and N_2 physisorption measurements (Micromeritics). Electrochemical impedance spectroscopy (EIS) was performed on an electrochemical workstation (CH Instruments) to evaluate the charge transfer resistance of the catalysts. Furthermore, electron paramagnetic resonance (EPR, Bruker A300) was utilized to detect and identify ROS generated during the catalytic process. Other analytical methods were summarized in Text S1.

2.4 Catalytic ozonation experiments and analysis methods

DEET degradation via catalytic ozonation was performed in a 250 mL batch reactor maintained at 25 °C. Ozone was generated using a COM-AD-01 ozone generator (Germany) and introduced continuously at a gas-phase concentration of 0.58 mg min^{-1} and a flow rate of 100 mL min^{-1}. Standard reaction conditions included an initial DEET concentration of 10 mg L^{-1}, catalyst loading of 0.1 g L^{-1}, stirring rate of 300 rpm, temperature of 25 °C, and an unadjusted initial pH of 5.5. At designated time intervals, samples were withdrawn, filtered through a 0.22 μm membrane, and analyzed for target compounds.

ROS were detected by electron paramagnetic resonance (EPR) spectroscopy using DMPO (5,5-dimethyl-1-pyrroline N-oxide) as a spin trap for hydroxyl radicals (·OH) and superoxide anions ($O_2^{\cdot-}$), and TEMP (2,2,6,6-tetramethyl-4-piperidinol hydrochloride) for singlet oxygen ($^1O_2$). Dissolved ozone (O_3) was quantified by iodometric titration (see Text S2 for details). Target pollutants—DEET, ibuprofen (IBP), primidone (PRM), atrazine (ATZ), and ketoprofen (KET)—were analyzed by high-performance liquid chromatography (HPLC) as described in Text S1. All experiments were performed in triplicate, and results are reported as mean ± standard deviation.

2.5 Kinetic model

The ozonation degradation mechanism of trace contaminants follows a dual-pathway route: (1) direct ozonation, where ozone molecules (O_3) undergo selective electrophilic reactions with the contaminants; and (2) free radical-mediated indirect oxidation (Xu et al. 2016a, 2022). Hydroxyl radicals (·OH) initiate non-selective chain reactions (Eq. (1)). During the experiment, excess ozone was continuously introduced to maintain a stable concentration of dissolved ozone in the liquid phase. Under this steady-state condition, the composite reaction rate constant (k_{cmb}) was derived using Eq. (2) to characterize the overall degradation rate of the contaminant in the presence of the catalyst. The apparent reaction rate constant (k_{app}) was calculated using Eq. (3). In all kinetic parameter calculations, the ozone concentration [O_3] was corrected using the time-weighted average (TWA) to eliminate the effect of instantaneous concentration fluctuations. Finally, by comparing the composite reaction rate constant (k_{cmb}) with the rate constant of the non-catalytic control system, the enhancement effect of the catalyst on the degradation rate of the contaminant was quantitatively evaluated.

$$-\ln\left(\frac{[DEET]_t}{[DEET]_0}\right) = \int_0^t \left(k_{O_3}\cdot[O_3] + k_{\cdot OH}\cdot[\cdot OH] + k_{O_2^{\cdot-}}\cdot\left[O_2^{\cdot-}\right]\right)dt \quad (1)$$

$$k_{app} = k_{cmb}\cdot[O_3] \quad (2)$$

$$-\ln\left(\frac{[DEET]_t}{[DEET]_0}\right) = k_{app}\cdot t \quad (3)$$

2.6 Density functional theory calculation

The computational method of density functional theory (DFT) is described in Text S2.

2.7 Toxicity assessment

Toxicological analysis was performed using T.E.S.T. software to evaluate the rat acute oral median lethal dose (LD_{50}), bioaccumulation factor (BCF), developmental toxicity, and mutagenicity of DEET and its degradation products. Bioavailability toxicity verification was carried out by collecting water samples from the degradation process (filtered through a 0.22 μm membrane) and assessing the inhibition rate of luminescence intensity in Vibrio fischeri, which was used as an indicator to quantitatively characterize changes in the overall toxicity of the water. A microplate luminescent bacterial assay was employed using Vibrio fischeri following ISO 11348. A dilution series of the filtered water samples (100–0.1%)

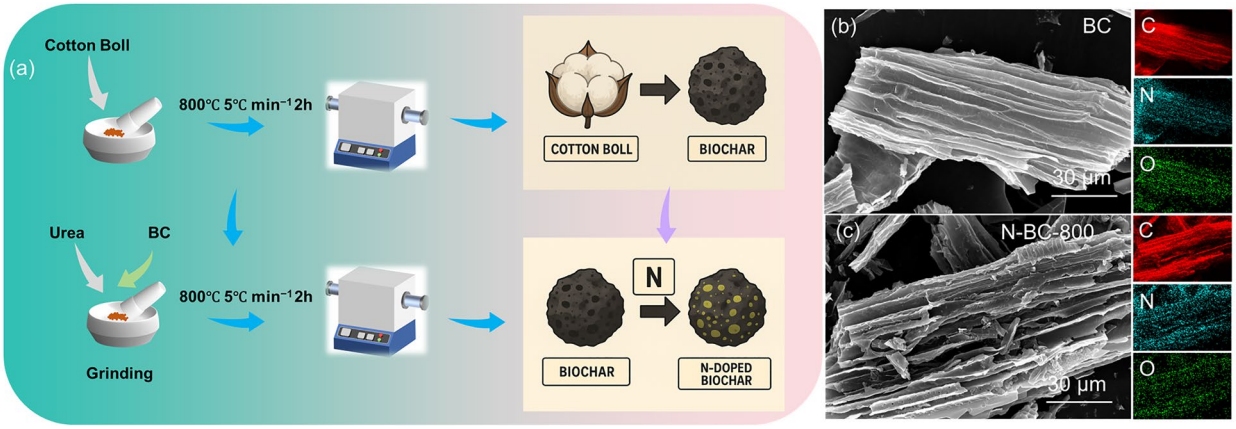

Fig. 1 **a** Schematic illustration of the synthesis process of BC and N-BC-800, **b** SEM images of BC and **c** N-BC-800

was prepared, and 50 μL of Vibrio fischeri was added to each tube and mixed thoroughly to avoid bubbles. The blank reference was set to 100% relative luminescence intensity. The assay was performed under temperature control at 25 °C, with luminescence measured at 470 nm for 15 min. The inhibition rate (IR%) was calculated and IC_{50} values were derived from the dose–response curves fitted by nonlinear regression. All data plots were generated using GraphPad Prism 8.

3 Results and discussion

3.1 Characteristics of N-BC-T

3.1.1 Morphology and element distribution

As shown in Fig. 1a, BC and N-BC-800 were prepared via a simple pyrolysis strategy. BC was synthesized through one-step pyrolysis, and N-BC-800 was synthesized by mixing urea with BC followed by pyrolysis. The morphological features of the catalysts were examined by scanning electron microscopy (SEM). As shown in Fig. 1b, the pristine biochar (BC) possessed a characteristic layered structure. This structural motif was largely preserved after nitrogen doping (Fig. 1c), with no significant morphological changes observed across pyrolysis temperatures ranging from 600 to 900 °C (Additional file 1: Fig. S1). These results indicate that nitrogen incorporation does not compromise the structural integrity of BC, and that elevated pyrolysis temperatures do not induce structural degradation. Energy dispersive X-ray spectroscopy (EDX) elemental maps further showed that the nitrogen signal in the N-BC-800 sample was significantly enhanced compared to BC, and the nitrogen element was uniformly distributed in the carbon matrix, which indicates successful nitrogen doping. High-resolution TEM imaging further corroborated the high crystallinity of N-BC-800, as evidenced by well-defined lattice fringes.

3.2 Physicochemical properties

The crystal structures of all materials were analyzed by X-ray Diffraction (XRD) (Fig. 2a). BC and N-BC amorphous and crystalline carbon peaks belonged to (002) and (100) facets, respectively (Ding et al. 2020). Other sharp peaks corresponded to $CaCO_3$ derived from biomass (JCPDS No. 87-1526).

The Fourier transform infrared (FTIR) spectrum (Fig. 2b) reveals an absorption peak at 3414 cm^{-1} corresponding to the stretching vibration of –OH groups (Zhou et al. 2022). A significant peak at 1566 cm^{-1} is attributed to the C=N stretching vibration in the nitrogen-doped material, indicating the successful incorporation of nitrogen into the carbon framework (Ouyang et al. 2019). Furthermore, an absorption peak at 1625 cm^{-1} corresponds to C=O vibrations (Duan et al. 2014), while a peak at 1378 cm^{-1} represents C–H vibrations. The C–N vibration peak at 1080 cm^{-1} is notably higher in the nitrogen-doped samples compared to BC (He et al. 2016), further demonstrating that, after high-temperature treatment and the removal of unstable groups, defect sites in the carbon skeleton are exposed, and nitrogen atoms anchor to these topological defects in the form of thermally stable heterocyclic nitrogen (Wan et al. 2020).

The intensity ratio of D band to G band (I_D/I_G) in Raman spectroscopy can effectively evaluate the degree of defects in carbon materials (Choi et al. 2012). As shown in Fig. 2c, the characteristic peaks located at 1352 cm^{-1} and 1558 cm^{-1} correspond to the defect-induced vibrational mode (D band) and in-plane stretching vibration (G band) in the sp^2 carbon structure, respectively (Wang et al. 2023b). The analysis indicates that the I_D/I_G ratio of nitrogen-doped biochar was significantly higher than that of undoped BC (1.046), confirming that nitrogen doping introduces more structural defects. The I_D/I_G ratio increased to a maximum and then decreased with

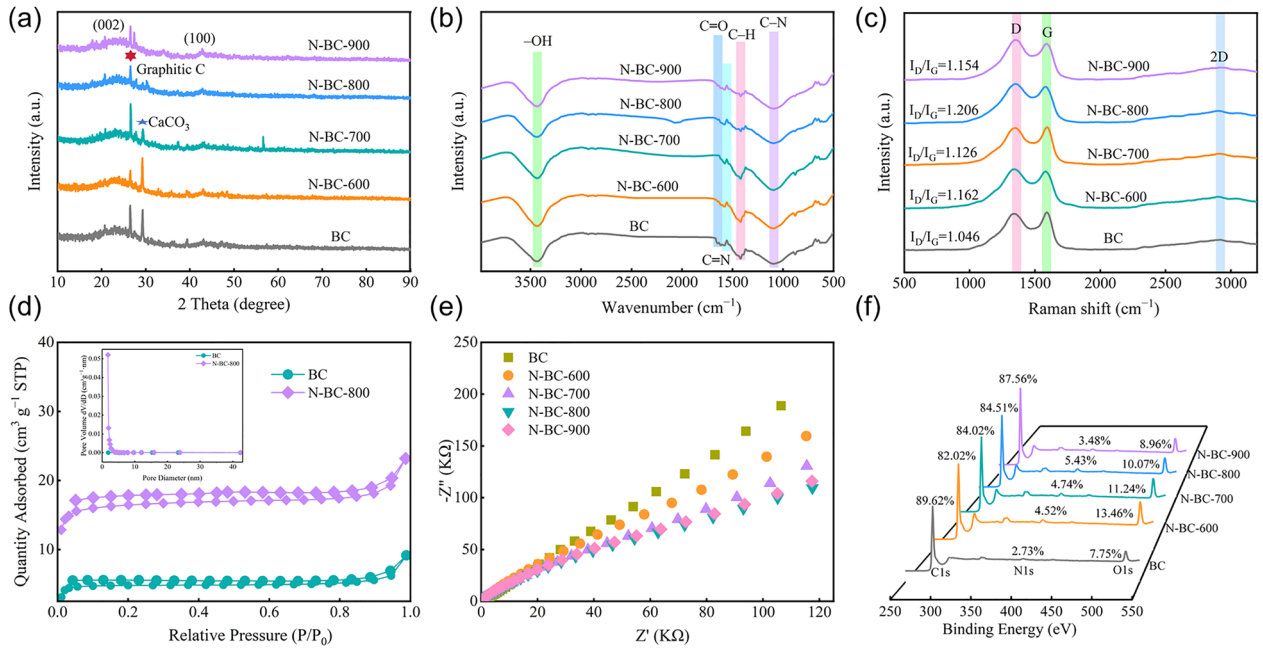

Fig. 2 **a** XRD patterns, **b** FTIR spectra, and **c** Raman spectra of BC, N-BC-600, N-BC-700, N-BC-800, and N-BC-900. **d** Adsorption–desorption isotherms of BC and N-BC-800. **e** EIS spectra and **f** XPS survey spectra of BC, N-BC-600, N-BC-700, N-BC-800, and N-BC-900

increasing pyrolysis temperature, with N-BC-800 having the highest ratio (1.206), indicating the highest degree of defects in the studied system. It is generally believed that oxygen and nitrogen-containing functional groups tend to be located at edge defect sites of carbonaceous materials, and defects are the key factors promoting O_3 decomposition (Wei et al. 2020). A higher I_D/I_G ratio confirms the presence of abundant edge and structural defects in the material, thereby enhancing its electron supply capability. Therefore, the high chemical potential and free electrons that may be induced by nitrogen doping can effectively promote O_3 decomposition and generate ROS (Banhart et al. 2010).

The specific surface area and pore size distribution were characterized by N_2 physisorption (BET method), with the results shown in Fig. 2d and Additional file 1: Table S3. The specific surface area of N-BC-800 was 66.13 $m^2\ g^{-1}$, and the total pore volume was 0.01094 $cm^3\ g^{-1}$, which were 3.35 times and 1.84 times higher than those of BC material (19.74 $m^2\ g^{-1}$, 0.00593 $cm^3\ g^{-1}$), and the average pore size was significantly reduced. The results show that nitrogen doping can effectively optimize the pore structure. These changes are attributed to lattice distortion and topological defects caused by nitrogen doping, which expose more internal pores. At the same time, nitrogen atoms stabilize the defect sites through covalent bonds, enhance the stability of the carbon layer, inhibit pore collapse, and promote the formation of hierarchical pore structure dominated by mesopores.

Electrochemical impedance spectroscopy (EIS) analysis revealed the electron transfer characteristics of the catalyst (Fig. 2e). Compared to pristine BC, the capacitive arc diameter of the nitrogen-doped catalyst was significantly reduced, indicating that the introduction of nitrogen significantly enhanced the charge transfer efficiency of the material. Among samples prepared at different pyrolysis temperatures, the N-BC-800 sample exhibited the smallest capacitive arc radius, indicating its optimal electron transfer performance within this catalyst series, thereby accelerating the decomposition of ozone for ROS generation (Yu et al. 2020).

The X-ray photoelectron spectroscopy (XPS) survey spectra (Fig. 2f) revealed a substantially higher nitrogen content in the doped samples compared to BC, which confirmed the effective incorporation of nitrogen. The nitrogen content reached a maximum at 800 °C and decreased with the continued increase of temperature. It might be attributed to thermal decomposition of nitrogen functional groups and subsequent formation of nitrogen-conjugated structures.

To clarify the chemical state of the catalyst surface, high-resolution X-ray photoelectron spectroscopy (XPS) was used for characterization (Fig. 3). The deconvolution of the C 1 s spectrum yielded four component peaks at binding energies of 284.8, 286.1, 287.1, and 288.8 eV, representing C–C/C=C (77.73%), C–O (7.76%), C–N (9.05%) and O–C=O (5.57%), respectively (Xu et al. 2016b). which confirmed that the carbon skeleton was

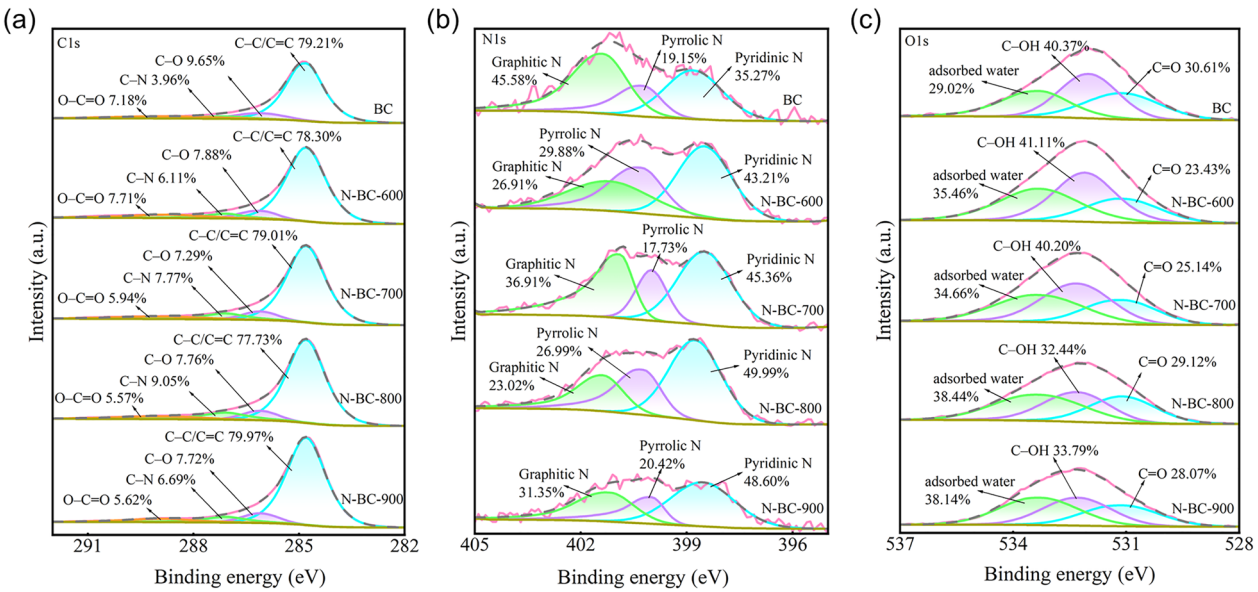

Fig. 3 High-resolution scanning XPS spectra of **a** C 1s, **b** N 1s, and **c** O 1s in BC, N-BC-600, N-BC-700, N-BC-800, and N-BC-900

mainly graphite structure. The N 1s spectra showed three characteristic peaks at 398.5, 400.3, and 401.2 eV, corresponding to pyridine type nitrogen (49.99%), pyrrole type nitrogen (26.99%) and graphite type nitrogen (23.02%), respectively (Duan et al. 2014), indicating that nitrogen was mainly in the pyridine type configuration. The O 1s spectrum showed three characteristic peaks at 531.1, 532.1, and 533.3 eV, corresponding to C=O bond (29.12%), –OH (32.44%) and adsorbed H_2O (38.44%), respectively (Jingjing et al. 2022), reflecting the rich hydroxyl and hydration characteristics of the catalyst surface.

A comparative analysis was conducted on catalysts with different pyrolysis temperatures and nitrogen doping levels. The results showed that the nitrogen-doped samples had fewer C–O and C=O functional groups than the original biochar material. This suggests that introducing nitrogen effectively eliminates unstable oxygen-containing functional groups. This finding is consistent with observations made using FTIR. Concurrently, the C–N content increased gradually with rising nitrogen doping levels, suggesting that nitrogen atoms may replace oxygen atoms or occupy defect sites within the carbon matrix. It is also interesting to note that the proportion of pyridinic N increased with temperature up to 800 °C, but then decreased at 900 °C, which is likely due to thermal decomposition. The results demonstrate that pyrolysis at 800 °C enhances the structural order of the carbon layer whilst promoting the insertion of nitrogen atoms into the hexagonal ring system. This process generates an abundance of pyridinic N sites that act as catalytic centres.

N-BC-800 exhibited high defect density, abundant pyridinic N, optimized pore structure, and enhanced electron conductivity. These structures were considered crucial for enhancing catalytic ozone oxidation performance. Its structural defects and pyridine nitrogen served as active centers for ozone adsorption and decomposition, promoting ROS generation by mediating electron transfer. Concurrently, the expanded specific surface area and hierarchical porosity facilitated mass transfer and enrichment of reactants, while the improved conductivity accelerated interfacial reaction kinetics. To directly validate how these structural advantages translated into catalytic performance, a series of catalysts were systematically evaluated for the catalytic ozone oxidation degradation of pollutants.

3.3 Catalytic performance of N-BC-800

This study systematically evaluated the catalytic performance of nitrogen-doped biochar using DEET as the target compound. Due to DEET's ozone-resistant degradation properties, its direct reaction rate with ozone is extremely low ($k_{O_3,DEET} = 40.8\ M^{-1}\ s^{-1}$), yet it exhibits high reactivity toward hydroxyl radicals ($k_{\cdot OH,DEET} = 1.18 \times 10^9\ M^{-1}\ s^{-1}$) (Xu et al. 2022). As shown in Fig. 4a, N-BC-800 exhibited less than 5% adsorption removal efficiency within 20 min, indicating very limited adsorption capacity. The removal rate remained stable at approximately 5% over the subsequent 30 min without further improvement (Additional file 1: Fig. S2), indicating that the system's contribution to pollutant removal primarily stems not from adsorption but from catalytic reactions.

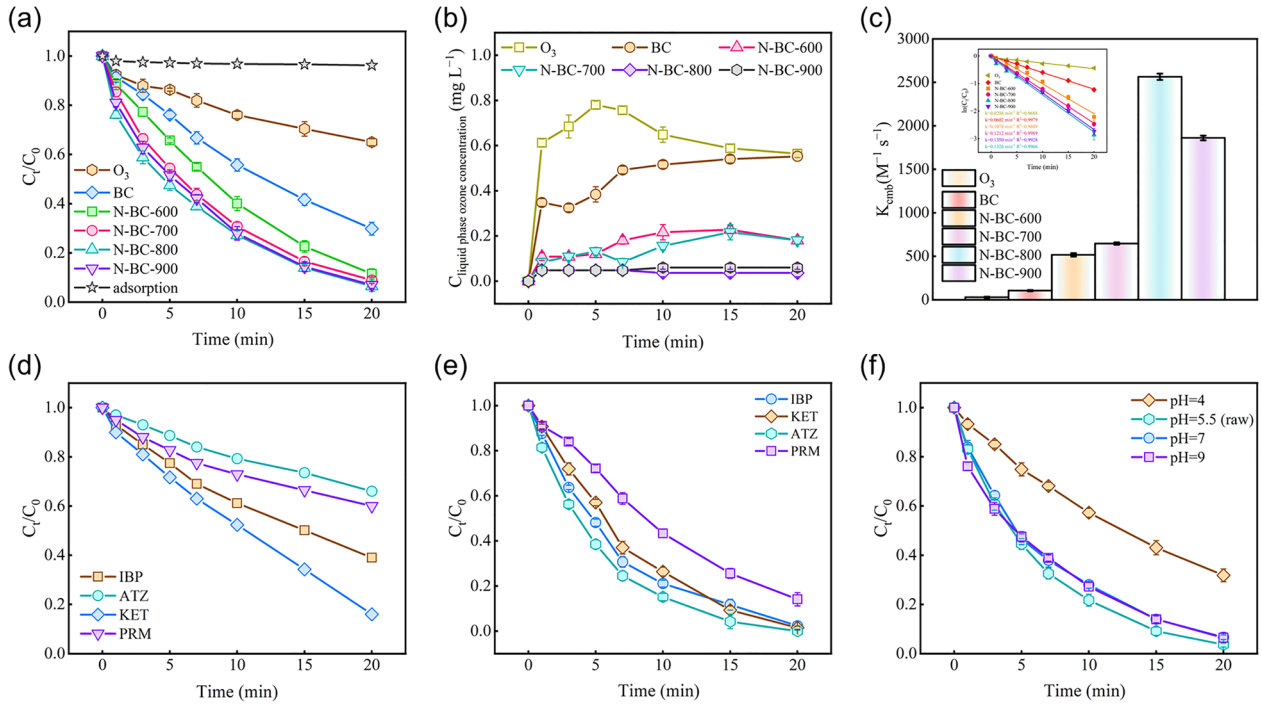

Fig. 4 BC and N-BC prepared at different calcination temperatures. **a** Catalytic degradation of DEET in the ozonation reaction, with corresponding **b** liquid-phase ozone concentrations and **c** apparent kinetic constants and secondary kinetic constants. **d** and **e** Removal tests of different organic pollutants by O_3 and O_3/N-BC-800. **f** Effect of pH on O_3/N-BC-800 system. Conditions: $[pollutants]_0 = 10$ mg L^{-1}, catalyst = 0.1 g L^{-1}, $[O_3]$ in gas = 0.58 mg min^{-1}, Temperature = 25 °C, pH 5.5 not adjusted

Compared to ozone alone, adding biochar resulted in only a slight improvement in degradation efficiency, suggesting limited catalytic activity of the biochar material. However, the addition of N-BC-800 elevated the treatment efficiency to 94%, demonstrating a significant improvement in performance. This indicates the material possesses outstanding catalytic capability.

Additionally, the ozone concentration in the liquid phase was measured (Fig. 4b), revealing that N-BC-800 exhibited the highest ozone utilization rate, indirectly reflecting its outstanding catalytic capability. The k_{cmb} was calculated from liquid phase ozone concentration and Eqs. (2) and (3). As shown in Fig. 4c, the apparent rate constant (k_{cmb}) of the O_3/N-BC-800 system reached 2538 M^{-1} s^{-1}, which was 106 times and 25 times higher than that of ozone alone (24 M^{-1} s^{-1}) and the O_3/BC system (100 M^{-1} s^{-1}), respectively. In addition, under different mass ratios, the degradation rate was fastest when the urea:BC ratio was 1:1 (Additional file 1: Fig. S3). At different pyrolysis temperatures, the k_{cmb} value of N-BC-800 was 5 times, 4 times and 1.4 times higher than that of N-BC-600, N-BC-700, and N-BC-900, respectively. The above results fully proved the excellent catalytic performance of the catalyst in the ozone treatment process.

Based on systematic characterization and performance analysis, the ozone degradation catalytic activity of N-BC-800 toward DEET was significantly enhanced, achieving a degradation rate constant of 2538 M^{-1} s^{-1}. This value represents a 106-fold increase over ozone alone and a 25-fold increase over BC, attributable to the multiple structural optimizations induced by doping. Nitrogen doping successfully introduced abundant structural defects alongside numerous catalytic nitrogen species and oxygen-containing functional groups. Concurrently, it optimized the material's physical structure, substantially increasing its specific surface area and forming a hierarchical pore system dominated by mesopores. Collectively, these factors endowed the material with exceptional catalytic activity. This fully validates the intrinsic connection between nitrogen doping, structural synergistic optimization, and performance enhancement.

In order to evaluate the broad-spectrum catalytic performance of N-BC-800, we selected four typical organic pollutants, including triazine herbicide atrazine (ATZ), nonsteroidal anti-inflammatory drugs ketoprofen (KET) and ibuprofen (IBP), and antiepileptic drug sodium valproate (PRM). These pollutants were selected because of their high distribution in the environment, ecological risks, and unique functional group structure

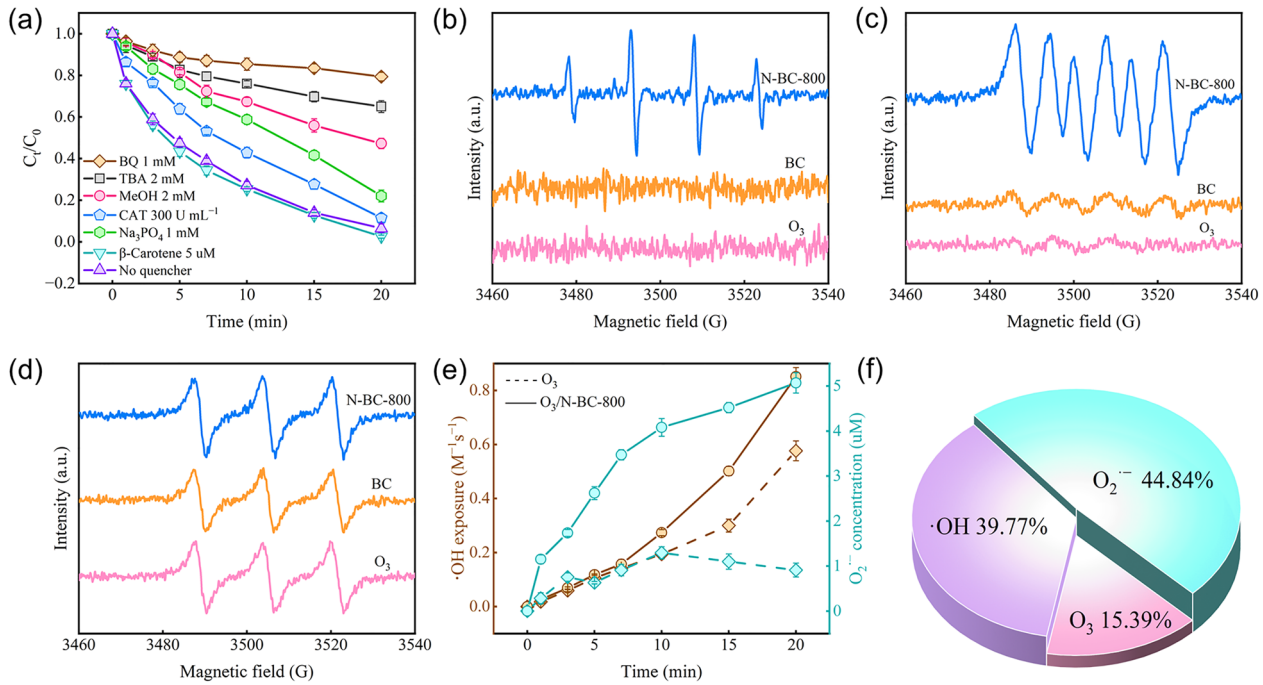

Fig. 5 **a** Quenching tests in the O_3/N-BC-800 system. EPR signals of **b** DMPO-·OH, **c** DMPO-$O_2^{\cdot-}$, and **d** TEMP-$^1O_2$ adducts in O_3, O_3/BC, and O_3/N-BC-800 systems. **e** Quantitative analysis of the ·OH and $O_2^{\cdot-}$ in O_3 and O_3/N-BC-800 systems. **f** Contribution ratios. Conditions: $[pollutants]_0 = 10$ mg L^{-1}, catalyst = 0.1 g L^{-1}, $[O_3]$ in gas = 0.58 mg min^{-1}, Temperature = 25 °C, pH 5.5 not adjusted, $[TBA]_0 = 2$ mM, $[BQ]_0 = 1$ mM, $[MeOH]_0 = 2$ mM, $[CAT]_0 = 300$ U mL^{-1}, $[\beta\text{-carotene}]_0 = 5$ mM

(triazine ring, carboxyl group and amide group, respectively). As shown in Fig. 4d–e, compared with ozone treatment alone, the removal rates of ATZ, KET, PRM, and IBP increased by 52%, 20%, 48% and 21%, respectively, in the O_3/N-BC-800 system, which fully proved its extensive catalytic efficiency. Ozone preferentially oxidizes electron-rich groups, so the electronic properties of pollutant functional groups determine their degradation activity. N-BC-800 promotes ozone decomposition to generate non-selective ROS, weakening structural selectivity and broadening the range of oxidizable species. Consequently, molecules containing carboxyl groups exhibit limited reactivity enhancement due to reduced ionization and electron-withdrawing effects. Nitrogen-containing structures, however, rely more heavily on ROS oxidation, resulting in significantly greater enhancement.

To further evaluate the comprehensive performance of N-BC-800, we compared the performance of nitrogen-doped carbon catalysts, typical metal oxides, and composite catalysts in ozone oxidation or other advanced oxidation systems (Additional file 1: Table S5), and plotted a comparison of their kinetic constants k (Additional file 1: Fig. S5). In this study, the O_3/N-BC-800 system exhibited relatively high kinetic constant ($k = 0.135$ min^{-1}) alongside excellent reusability (approximately 80% activity retention after five cycles). This indicates that N-BC-800 possesses both outstanding catalytic efficiency and stability compared to similar catalysts and common catalysts. Collectively, these results demonstrate that N-BC-800 not only enhances ozone utilization but also efficiently and broadly degrades pollutants with diverse structural characteristics.

The effect of pH on DEET degradation was also examined (Fig. 4f). Experiments designed under conditions of pH = 4.5–9.0 revealed high treatment efficiency across a broad pH range, with only a slight decrease at pH 4.5. This may be attributed to the limited ozone solubility under acidic conditions (Kosak et al. 1983). However, the degradation efficiency under this condition remained higher than that achieved with ozone or BC alone, further demonstrating the material's excellent pH adaptability.

3.4 Pyridinic N and C=O groups synergistically promote ROS generation.

3.4.1 Catalytic active species of N-BC-800

To investigate the removal effect of reactive oxygen species on DEET, quenching experiments were conducted (Fig. 5a). The results demonstrated that adding the superoxide radical ($O_2^{\cdot-}$) quencher benzoquinone (BQ) to the system caused the degradation efficiency of the target compound to plummet from 96% to 22% (Zhao et al. 2022). This finding strongly confirms that superoxide

radicals are one of the primary active species involved in the degradation process. Using methanol and tert-butanol (TBA) as hydroxyl radical quenchers yielded comparable results (Wang et al. 2020a). Upon adding tert-butanol to the system, the degradation efficiency significantly decreased to 35%; when methanol served as the hydroxyl radical (·OH) quencher, the efficiency dropped to 55%. Both findings confirm the crucial role of hydroxyl radicals in the degradation process. Furthermore, adding hydrogen peroxide (H_2O_2) quencher catalase (CAT) did not significantly alter degradation efficiency (Fotiou et al. 2016), indicating limited H_2O_2 activity in the system. Similarly, adding singlet oxygen ($^1O_2$) quencher β-carotene did not inhibit degradation efficiency, suggesting the absence of singlet oxygen in the system.

The generation of reactive oxygen species from the catalyst was monitored using the EPR technique. As shown in Fig. 5b–c, test results indicated that no distinct DMPO-·OH or DMPO-$O_2^{\cdot-}$ characteristic signals were detected in either the O_3 or O_3/BC systems alone. However, in the O_3/N-BC-800 system, a characteristic quadruplet peak with an intensity ratio of 1:2:2:1 was observed. This signal was assigned to the DMPO-·OH adduct, confirming the generation of hydroxyl radicals (Zhou et al. 2022). Concurrently, the characteristic sextet peak specific to DMPO-$O_2^{\cdot-}$ also appeared in this system, indicating the coexistence of superoxide radicals. In addition to ROS, singlet oxygen ($^1O_2$) is another form of reactive oxygen that frequently accompanies radical oxidation. As shown in Fig. 5d, compared to the O_3 control group, the intensity of the triple characteristic signal for TEMP-$^1O_2$ did not increase in the O_3/BC and O_3/N-BC-800 systems, indicating that singlet oxygen was not generated in these systems. The above quenching experiments and EPR analyses showed that ·OH and $O_2^{\cdot-}$ are the main ROS in the system. The roles of reactive oxygen species were further supported by in situ infrared characterization. DRIFTS results (Additional file 1: Fig. S16) revealed the dynamic evolution of $O_3^{\cdot-}$, $O_2^{\cdot-}$, and ·OH during ozone treatment. These findings demonstrated that N-BC-800 catalyzes the generation of $O_2^{\cdot-}$ and ·OH from ozone.

To further elucidate the role of various ROS in the degradation of DEET within the O_3/N-BC-800 system, the quantitative analysis using probe compounds was performed. 4-chlorobenzoic acid (pCBA) was used to detect ·OH, and nitroblue tetrazole chloride (NBT) was used to detect $O_2^{\cdot-}$ (Wang et al. 2023a). The results showed that compared with the ozone system alone, the ·OH exposure of O_3/N-BC-800 system increased by 46%, and the $O_2^{\cdot-}$ accumulation increased by 5.6 times (Fig. 5e). The contribution analysis further clarified the relative importance of DEET degradation pathways: $O_2^{\cdot-}$ (48.21%) > ·OH (36.40%) > direct ozone oxidation (15.39%) (Fig. 5f). These results clearly confirmed that $O_2^{\cdot-}$ was the main active substance in the degradation process, and ·OH was the key synergy.

3.4.2 Catalytic active sites of N-BC-800

Different nitrogen-doped species play distinct roles in the catalytic ozone oxidation process. Pyridinic N, owing to its lone pair electrons located at edges or defects, strongly adsorbs and promotes the spontaneous dissociation of ozone (Xiong et al. 2023). It primarily facilitates the generation of surface-adsorbed oxygen atoms and free peroxy species, thereby significantly accelerating radical chain reactions dominated by ·OH. In contrast, pyrrolic N exhibits weaker direct ozone activation capabilities (Sun et al. 2019). Its primary function lies in enhancing the apparent reaction rate by strengthening the interfacial adsorption and enrichment of pollutants. Alternatively, within specific material systems, it acts as a synergistic site that modulates the local electronic environment and aids in ·OH generation (Zeng et al. 2024). Graphitic N plays a central role by significantly altering the electronic structure of the carbon framework, endowing adjacent carbon atoms with high charge density and transforming them into active sites for efficient ozone adsorption and dissociation (Xu et al. 2020). Simultaneously, graphitic N significantly promotes interfacial electron transfer, serving as a key factor governing non-radical oxidation reactions (direct electron transfer) (Zhu et al. 2022). Furthermore, the C=O group, as an electron-rich site, is often recognized as a crucial active site for triggering non-radical reactions and generating various ROS.

To identify the key active sites of N-BC-800 in the catalytic ozonation process, this study systematically analyzed the correlation between the functional group composition on the catalyst surface and the DEET degradation kinetics (Fig. 6a). Correlation results indicated a significant positive correlation between the apparent reaction rate constant (k_{cmb}) and the relative content of C=O and pyridinic N groups. Additionally, C–N groups also correlate with the apparent reaction rate constant, though to a slightly lesser extent. Literature indicates that pyridinic N can contribute its π electrons to the conjugated system, enhancing the material's electron-donating ability. This facilitates electron transfer to oxidants and promotes ROS generation (Yang et al. 2022). Simultaneously, C=O groups have been reported to promote ozone activation, induce ROS generation, and enhance electron transfer in similar systems (Wang et al. 2018), further driving ozone decomposition to produce radicals such as ·OH or $O_2^{\cdot-}$ (Song et al. 2019b). In contrast, –OH, –COOH and graphitic N showed negative correlations

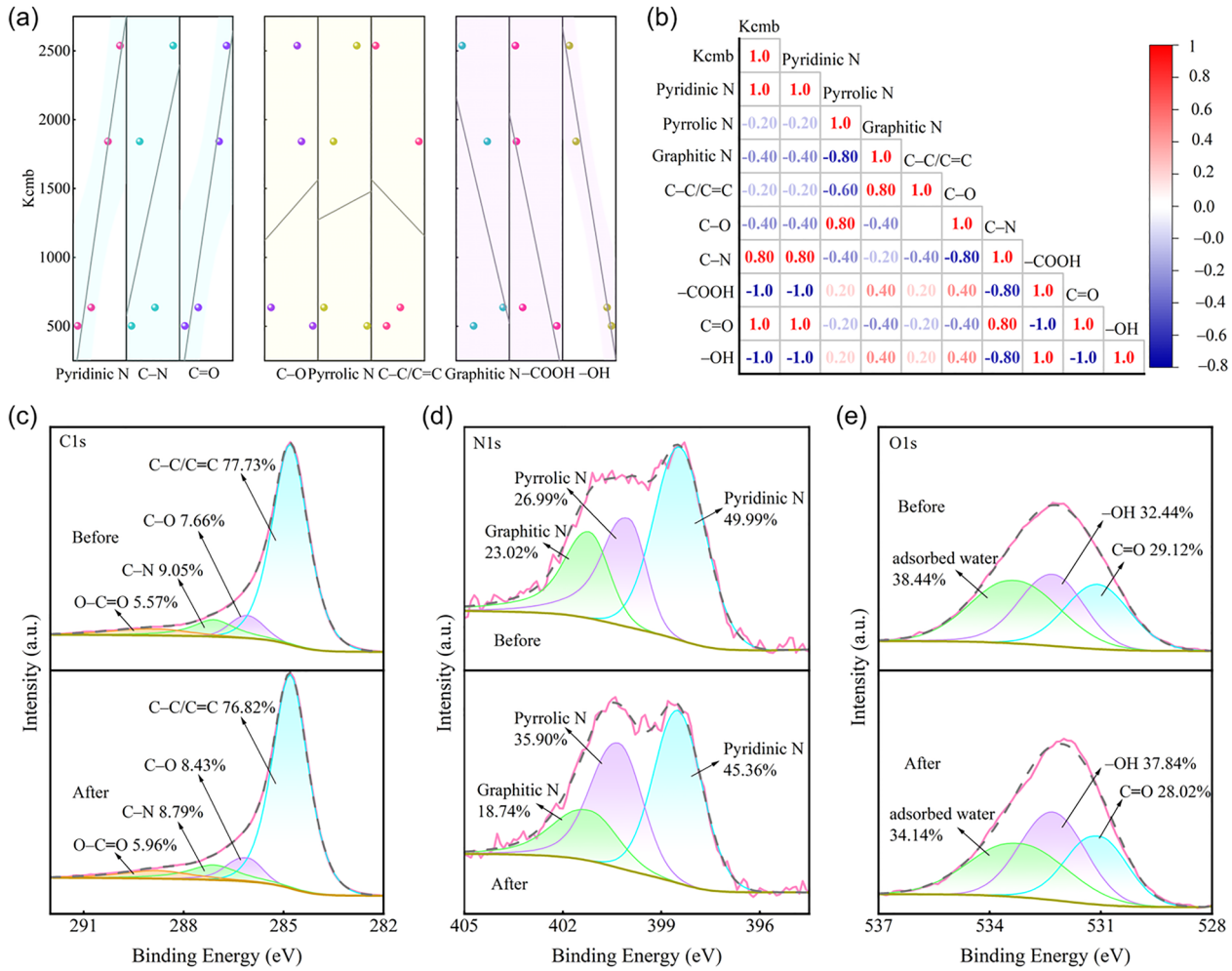

Fig. 6 **a** Correlation between the content of various groups and the DEET degradation rate during the catalytic ozonation process of N-BC-800 at different calcination temperatures. **b** Contribution of each group to DEET degradation, XPS fine spectra of **c** C1s, **d** N1s, and **e** O1s before and after the reaction

with k_{cmb}, while other functional groups like C–C/C=C, C–O, and pyrrolic N exhibited weaker influences. Collectively, C=O and pyridinic N are likely the most probable active sites in the N-BC-800-catalyzed ozonolysis process.

In order to investigate the mechanism of active sites, Spearman correlation analysis was further employed to systematically evaluate the correlation between various functional groups in catalyst k_{cmb} (Fig. 6b). The red and blue areas in the heat map represent the positive and negative correlations, respectively, and the depth of the color reflects the strength of the correlation. The analysis results indicated a significant positive correlation between pyridinic N and the C=O functional group.

Pre-reaction accurate XPS spectra further elucidated the active sites (Fig. 6c–e). Before and after the reaction, the pyridinic N content decreased from 49.99% to 45.36%, and the C=O content decreased from 29.12 to 28.02%. It was further confirmed that C=O and pyridinic N were active sites. In summary, the C=O and pyridinic N groups are the primary active sites, and synergistic interactions may also exist between them.

3.4.3 Synergistic mechanism of the O_3/N-BC-800 System

To investigate the mechanism of action of the active sites (C=O and pyridinic N groups) identified in the exploratory experiments during the catalytic reaction, this study employed density functional theory for computational analysis (Fig. 7). The results indicated that the adsorption energies of ozone molecules on the pyridinic N and C=O sites were −1.61 eV and −0.40 eV, respectively. This confirmed that both sites are capable of spontaneous chemisorption with ozone. Notably, when pyridinic N and C=O coexisted in a neighboring configuration

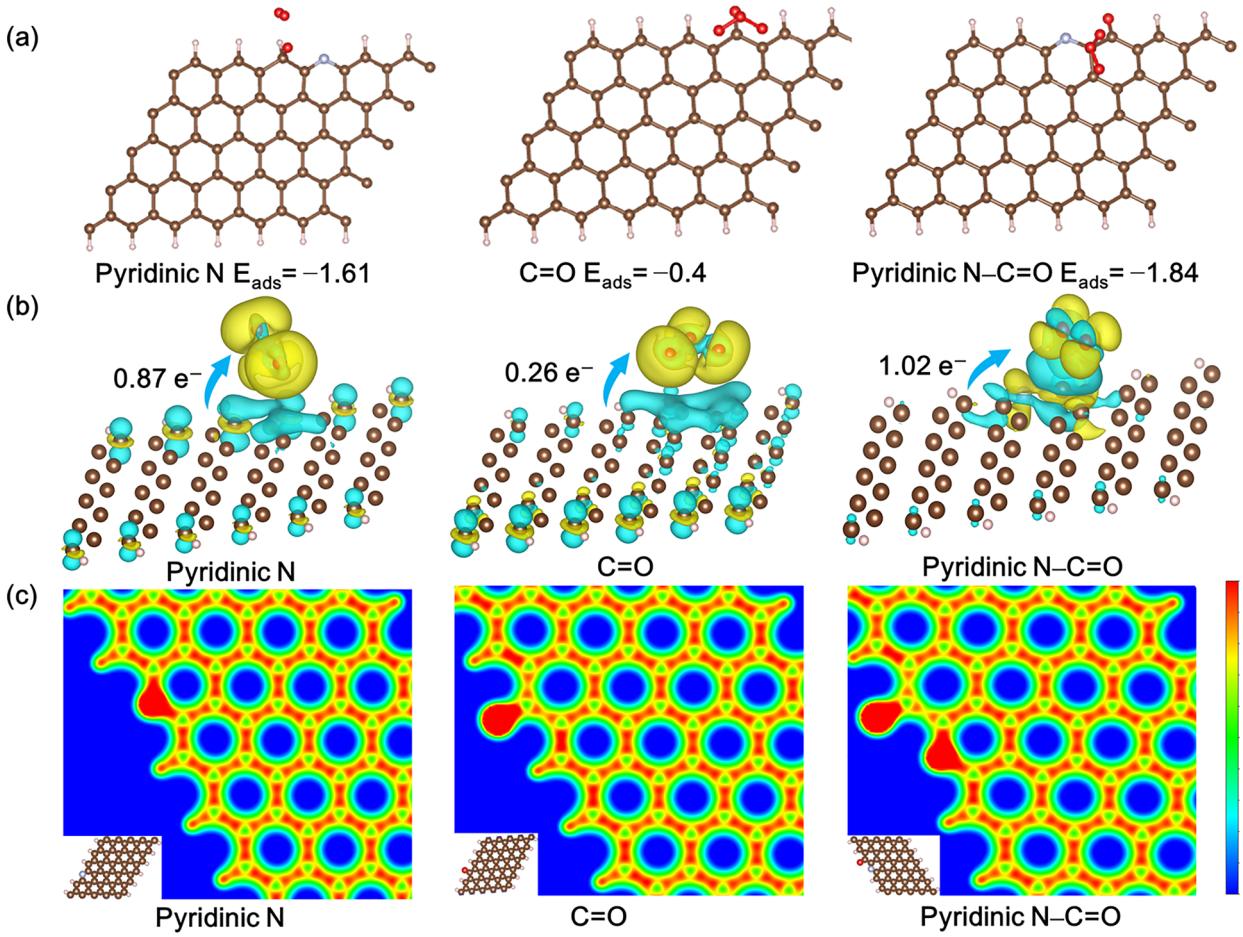

Fig. 7 **a** Adsorption energy of ozone molecules adsorbed on the pyridinic N, C=O, and pyridinic N–C=O groups on the surface of N-BC-800. **b** Differential charge density map of charge analysis on pyridinic N, C=O, and pyridinic N–C=O (blue regions indicate electron depletion; yellow regions indicate electron accumulation). **c** Charge density distribution in the presence of pyridinic N, C=O, and pyridinic N–C=O

(Fig. 7a), the ozone adsorption energy further decreased to −1.84 eV, indicating the strongest adsorption/activation capability among the three models. Furthermore, at the pyridinic N sites, the O–O bond of adsorbed ozone molecules undergoes significant stretching or even breaking, indicating efficient activation and conversion of ozone into highly reactive intermediates. Consistent with the more negative adsorption energy, the pyridinic N–C=O cooperative site exhibits an even stronger interaction with ozone, implying a more pronounced tendency toward ozone activation and subsequent transformation into reactive intermediates. These intermediates can subsequently react with water molecules or surface hydroxyl groups to generate ·OH, thereby significantly enhancing the system's oxidative capacity. Notably, the role of pyridinic N as an active site for ozone activation is consistent with findings in other heteroatom-doped carbon systems. For instance, studies on N-doped nanocarbons have also highlighted pyridinic N as a key "radical-generation" site that facilitates O–O bond cleavage and promotes ·OH formation through redox processes (Sun et al. 2019). Moreover, similar mechanistic roles have been observed for other heteroatoms such as phosphorus and boron, where doping-induced charge redistribution enhances ozone adsorption and decomposition (Wang et al. 2019b).

Bader charge analysis further corroborated these findings, revealing that ozone molecules adsorbed on pyridinic N and C=O sites acquired 0.87 and 0.26 electrons, respectively. Importantly, ozone adsorbed on the pyridinic N–C=O cooperative site gained 1.02 electrons (Fig. 7b), demonstrating the highest electron transfer capacity and further supporting its superior ozone activation efficiency. This data aligns closely with adsorption energy trends, revealing a clear structure–activity relationship between adsorption strength and electron

transfer capacity. More negative adsorption energies indicate stronger electron-donating ability of the site to ozone, leading to higher ozone activation efficiency. The charge-density difference isosurfaces in Fig. 7b also visually confirm this electron transfer behavior, with electron accumulation/depletion regions concentrated at the ozone-active-site interface, and the most pronounced redistribution occurring for the pyridinic N–C=O model. In addition, the 2D electronic distribution maps in Fig. 7c indicate that the reactive region is preferentially localized around defect/edge areas, and the pyridinic N–C=O configuration exhibits a more intense localized response than the single-site models, further evidencing the synergistic enhancement of interfacial activation. To address whether internal sites or isolated functional groups away from edges may also contribute, we further constructed additional structural models in which C=O and/or pyridinic N were positioned in the interior region and/or not in a neighboring arrangement (Additional file 1: Fig. S26). The new calculations showed that, compared with the edge-adjacent pyridinic N–C=O pair, these internal/separated configurations generally exhibited weaker ozone adsorption and less pronounced interfacial charge redistribution, suggesting a reduced tendency for direct O–O bond weakening/cleavage. Mechanistically, such internal or isolated groups are still able to chemisorb ozone and may serve as auxiliary "capture/enrichment" centers that increase local ozone residence time and facilitate subsequent migration/activation at more reactive defect/edge domains; however, efficient radical-generation is expected to preferentially occur at exposed defect/edge environments where electronic states are more localized and the cooperative donor-polarization effect can be maximized. Based on the strengthened adsorption and enhanced interfacial electron transfer, we clarified that the neighboring pyridinic N–C=O pair functions as a coupled donor-polarization unit. Pyridinic N primarily contributes electron donation to ozone, while the adjacent C=O modulates/polarizes the local electronic environment, stabilizing charge rearrangement and facilitating greater electron population on ozone—hereby promoting O–O bond weakening/cleavage and subsequent formation of reactive oxygen intermediates, which then drive ·OH generation.

To further provide experimental evidence for the synergy between pyridinic N and C=O, we performed selective site-passivation/control experiments (Additional file 1: Fig. S27-S29). The results showed that when the catalyst surface was modified to retain only a single type of active site (either pyridinic N or C=O), the catalytic activity decreased markedly. In contrast, the catalyst preserving both functionalities exhibited a higher reaction rate and stronger oxidative capacity. These observations demonstrate that, compared with isolated single sites, the neighboring pyridinic N–C=O cooperative site more efficiently activates ozone and promotes the generation of ROS, thereby significantly enhancing catalytic performance. This experimental evidence is in good agreement with our DFT results, which indicate strengthened adsorption/charge transfer and facilitated O–O bond weakening/cleavage at the cooperative pyridinic N–C=O site.

In comparison with other oxygen-containing functional groups reported in heteroatom-doped carbons, the C=O group in this study exhibits a relatively moderate adsorption energy but still plays a crucial role in ozone activation. This aligns with previous reports that electron-rich oxygen groups on carbon surfaces can act as Lewis basic sites to promote ozone decomposition and ·OH generation, albeit often to a lesser extent than nitrogen dopants when both are present (Ta et al. 2024).

To experimentally verify that C=O sites promote ROS generation rather than merely serving as weak adsorption sites, we controlled the composition of active sites through muffle furnace calcination. XPS analysis of the calcined samples (Additional file 1: Fig. S11) revealed that pyridine nitrogen content decreased to 1.26% (equivalent to BC), while C=O content significantly increased from 2.93% to 7.94%. Notably, despite the reduced pyridine nitrogen content, calcined samples exhibited enhanced DEET degradation kinetics (Additional file 1: Fig. S12), directly demonstrating that enriched C=O groups significantly promote ozone activation and ROS-mediated pollutant degradation. Consistent with this, radical identification and quantitative analysis further indicated that C=O enrichment markedly increased ROS production (Additional file 1: Fig. S13 and S14). Quenching experiments revealed that compared to uncalcined materials, calcined N-BC-800 exhibited significantly enhanced inhibition of DEET degradation upon addition of BQ. Further quantitative testing revealed markedly higher concentrations of $O_2^{\cdot-}$ generated on the material's surface. These findings directly demonstrate that C=O groups formed on the surface during calcination effectively promote $O_2^{\cdot-}$ generation, thereby enhancing the superoxide radical-based catalytic oxidation pathway. Notably, despite the relatively weaker direct adsorption and electron transfer capabilities of the C=O group, it plays a crucial role in the catalytic system. It can activate ozone into the ozonide anion through specific electron transfer pathways, a species that serves as a key precursor for ·OH generation. Simultaneously, adsorbed ozone can also be activated into superoxide radicals, collectively promoting the efficient progression of the catalytic oxidation process.

As shown in Fig. 8, supported by experimental results and DFT calculations, a mechanism for DEET

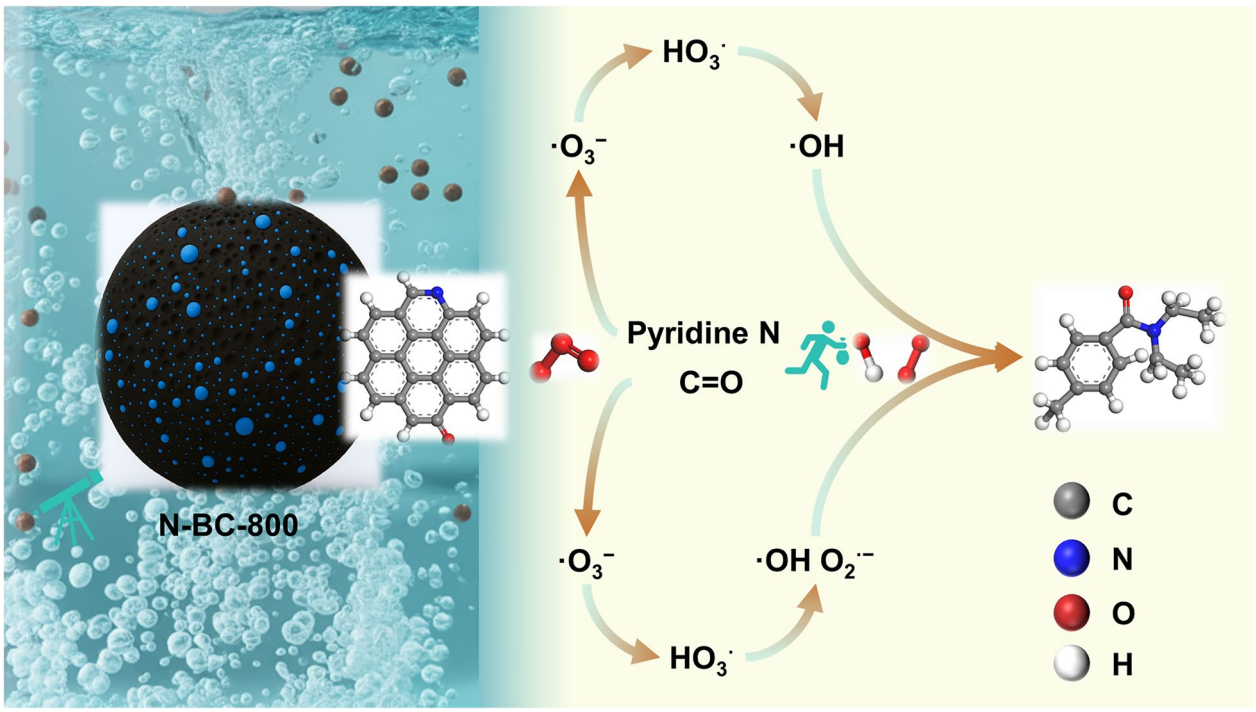

Fig. 8 Mechanism diagram of DEET degradation in the O_3/N-BC-800 system

degradation in the O_3/N-BC-800 system is proposed. In this system, the primary catalytic active sites are C=O groups and pyridinic N. Their interactions generate abundant ROS species such as ·OH and $O_2^{\cdot-}$. Specifically, pyridinic N acts as an efficient electron donor, transferring electrons to adsorbed ozone molecules to generate $\cdot O_3^-$ as shown in Eq. (4). $\cdot O_3^-$ subsequently forms $HO_3\cdot$ (Eq. (5)) (Sui et al. 2010) and rapidly converts to ·OH (Eq. (6)) (Xiao et al. 2017). The C=O group and ozone convert to ·OH and $O_2^{\cdot-}$ (Eqs. (7) and (8)) (Wang et al. 2020b), with $\cdot O_3^-$ subsequently forming $HO_3\cdot$ (Eq. (4)) and rapidly converting to ·OH (Eq. (5)) (Song et al. 2019a). Finally, the generated reactive oxygen species can diffuse into the bulk solution, thereby contributing to DEET removal.

$$\text{N - BC - 800 - pyridineN} + O_3 + e^- \leftrightarrow \cdot O_3^- \quad (4)$$

$$\cdot O_3^- + H_2O \leftrightarrow HO_3\cdot \quad (5)$$

$$HO_3\cdot \leftrightarrow O_2 + \cdot OH \quad (6)$$

$$N - BC - 800 - C = O + O_3 \leftrightarrow O_2^{\cdot-} \quad (7)$$

$$N - BC - 800 - C = O + O_3 \leftrightarrow \cdot O_3^- \quad (8)$$

3.5 Stability and reusability of N-BC-800

To evaluate the catalytic performance of N-BC-800 under different environmental conditions, we examined the effects of natural organic matter (NOM) and common inorganic anions (SO_4^{2-}, Cl^-, and HCO_3^-) on DEET degradation (Fig. 9a–b). The results showed that NOM or SO_4^{2-}/Cl^- did not significantly affect the degradation efficiency. In contrast, HCO_3^- exhibits a slight inhibitory effect, which can be attributed to its bicarbonate reacting with hydroxyl radicals to generate weakly oxidizing carbonate radicals (Yang et al. 2015). In actual water substrates, the characteristics of the actual aqueous matrix are shown in Additional file 1: Table S4. In municipal wastewater treatment plant effluent and river water, the initial degradation rate of DEET showed a slight decline, possibly due to the competitive consumption of ozone and ROS by background components (Fig. 9c). However, the final removal efficiency was still comparable to that observed in ultrapure water. The above results indicate that N-BC-800 can maintain good catalytic activity in different water substrate environments.

Further analysis of dissolved organic matter (DOM) in real water was performed using three-dimensional fluorescence spectroscopy (EEM). The results showed that DOM is mainly composed of aromatic proteins,

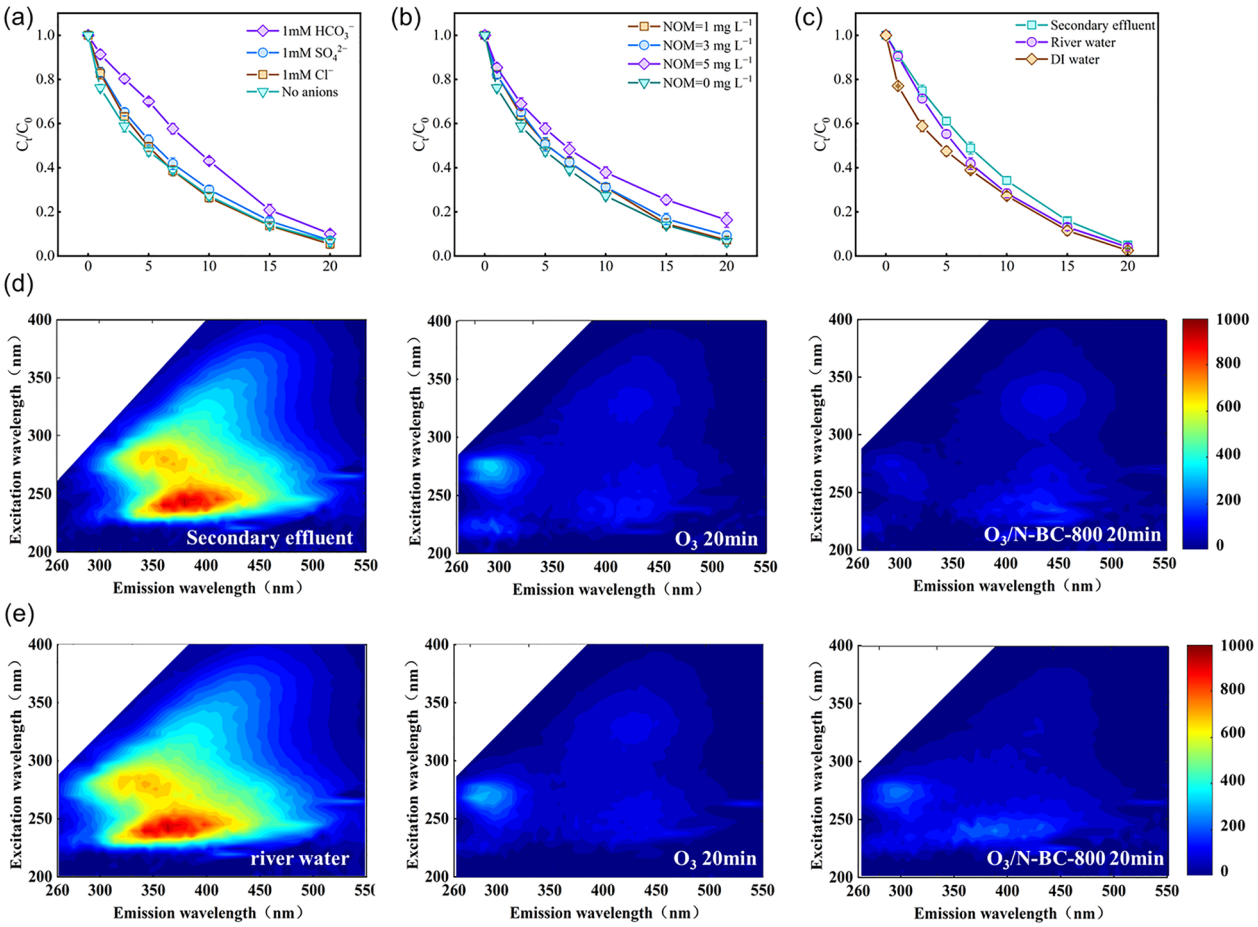

Fig. 9 The effect of **a** NOM, **b** inorganic anions, and **c** different substrate water qualities on degradation efficiency, **d** secondary city effluent, and **e** three-dimensional fluorescence spectrum of river water

microbial metabolites, and fulvic acid like substances (Fig. 9d–e). After treatment with the O_3/N-BC-800 system, the fluorescence intensity in all regions was significantly reduced, and the decomposition efficiency of fulvic acid-like substances and microbial-derived compounds was significantly improved. At the same time, the increase in T/C indicates an enhanced biodegradability of the water body (Additional file 1: Fig. S6 a-d). In summary, N-BC-800 can still maintain high catalytic activity in actual water bodies.

Further evaluation of conventional water quality parameters showed that the removal rates of total organic carbon TOC and chemical oxygen demand COD in the secondary effluent increased from 28% and 35% to 50% and 42%, respectively, while the removal rates in river water increased from 46% and 50% to 58% and 56% (Additional file 1: Fig. S6 e–f). Compared with using ozone alone, the O_3/N-BC-800 system significantly improved the removal efficiency of TOC and COD. The stability test of the catalyst showed that N-BC-800 maintained about 80% of its catalytic activity after five consecutive reaction cycles. XRD analysis before and after the reaction confirmed that no new phases were observed (Additional file 1: Fig. S7 a-b). Using secondary effluent as the aqueous medium, N-BC-800 retained approximately 73% of its catalytic activity after five consecutive reaction cycles. XRD analysis before and after the reaction confirmed no formation of new phases (Additional file 1: Fig. S8 and S9), indicating that the catalyst has excellent reusability and structural stability. In summary, these results indicate that N-BC-800 is an efficient and durable catalyst that can adapt to complex water matrices and achieve efficient removal of pollutants and improved effluent biodegradability under realistic environmental conditions.

3.6 Degradation pathways and toxicity reduction of DEET

Positive ion mode analysis by liquid chromatography-mass spectrometry (LC–MS) showed that 14 intermediate products were produced during the degradation of DEET in the O_3/N-BC-800 system (Additional file 1: Table S8). The spectra of the formed DEET products are shown in Additional file 1: Fig. S17-S25.These transformation products are classified into four structural types, including hydroxylated derivatives, dealkylated products, decarboxylated products, and oxidized ring opening derivatives. Based on these intermediates, researchers proposed seven degradation pathways (Fig. 10).

Pathway 1 begins with the oxidation of DEET to generate P2, followed by decarboxylation to form P5, and then hydroxylation reaction to generate P11. In pathway 2, P5 continues to decarboxylate to form P7, followed by continuous hydroxylation steps to form P8, P9, and P10 in sequence. Pathway 3 directly decarboxylates DEET to generate P1. Pathway 4 generates P6, P12, and P13 through stepwise hydroxylation. Pathway 5 starts from P12 and undergoes additional hydroxylation to form P14. Pathway 6 starts with the hydroxylation of DEET to generate P4, followed by decarboxylation reaction. Finally, pathway 7 directly generates P3 through demethylation. All intermediate products ultimately undergo gradual oxidation and are fully mineralized into CO_2 and H_2O.

Toxicity assessment was conducted using the US Environmental Protection Agency's toxicity assessment software tool (T.E.S.T.) to systematically evaluate acute toxicity (oral LD_{50} in rats), bioaccumulation factor (BCF), developmental toxicity, and mutagenicity (Fig. 11a–d, Tables S5 and S6). Compared to the parent compound DEET (LD_{50} = 1749.4 mg kg^{-1}, classified as moderate toxicity), the acute toxicity of most intermediate products is significantly reduced. The BCF values of all transformation products are significantly low, indicating that their bioaccumulation potential is minimal. In the assessment of developmental toxicity, intermediate products P1, P9, P10, and P14 were predicted to be non-toxic, while the remaining products were predicted to only pose slight developmental risks. It is worth noting that neither mosquito repellent nor its transformation products have been predicted to have mutagenicity.

To verify these predictions, a bioluminescence inhibition experiment of Vibrio fischeri was conducted using the treated solution (Fig. 11e). Compared with 44% observed with ozone alone, the O_3/N-BC-800 system showed significantly lower inhibition rates, with inhibition rates of 22% at 10 min and 16% at 20 min, confirming the excellent effect of catalytic treatment in reducing residual bioavailable toxicity.

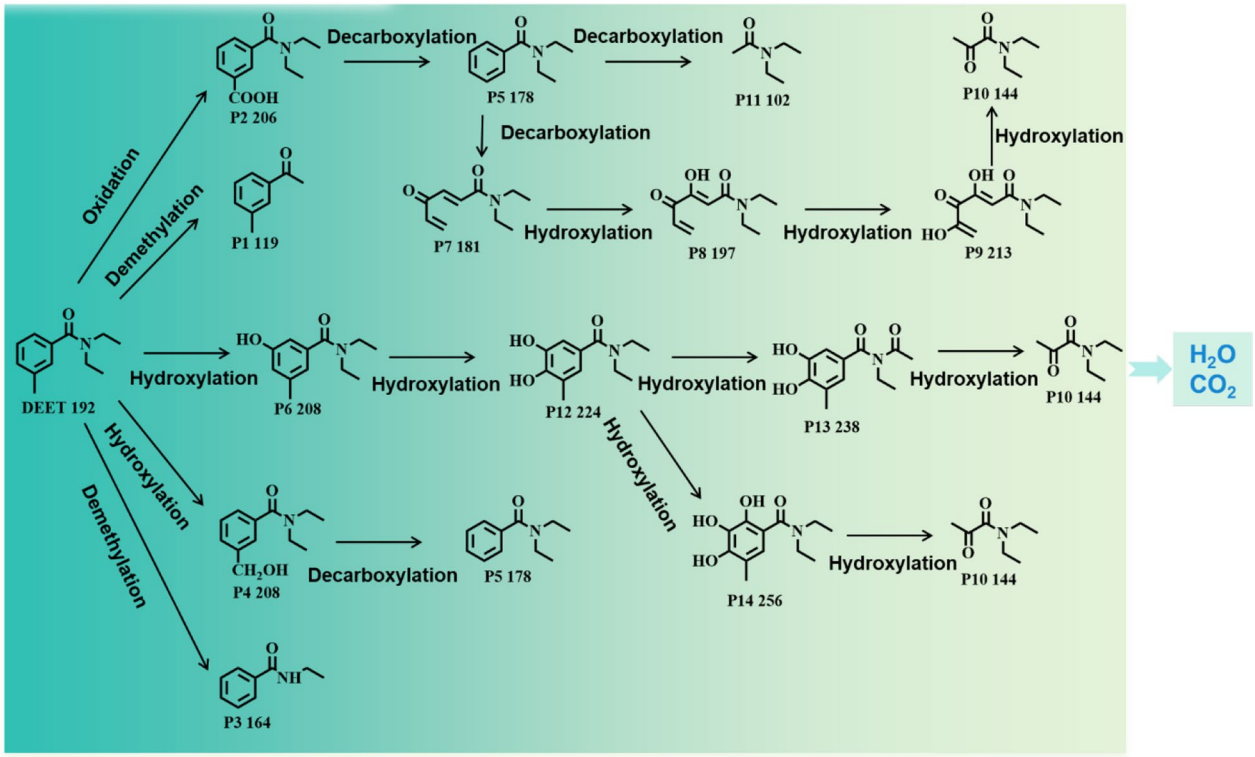

Fig. 10 Degradation pathway of N-BC-800-catalyzed ozone degradation of DEET

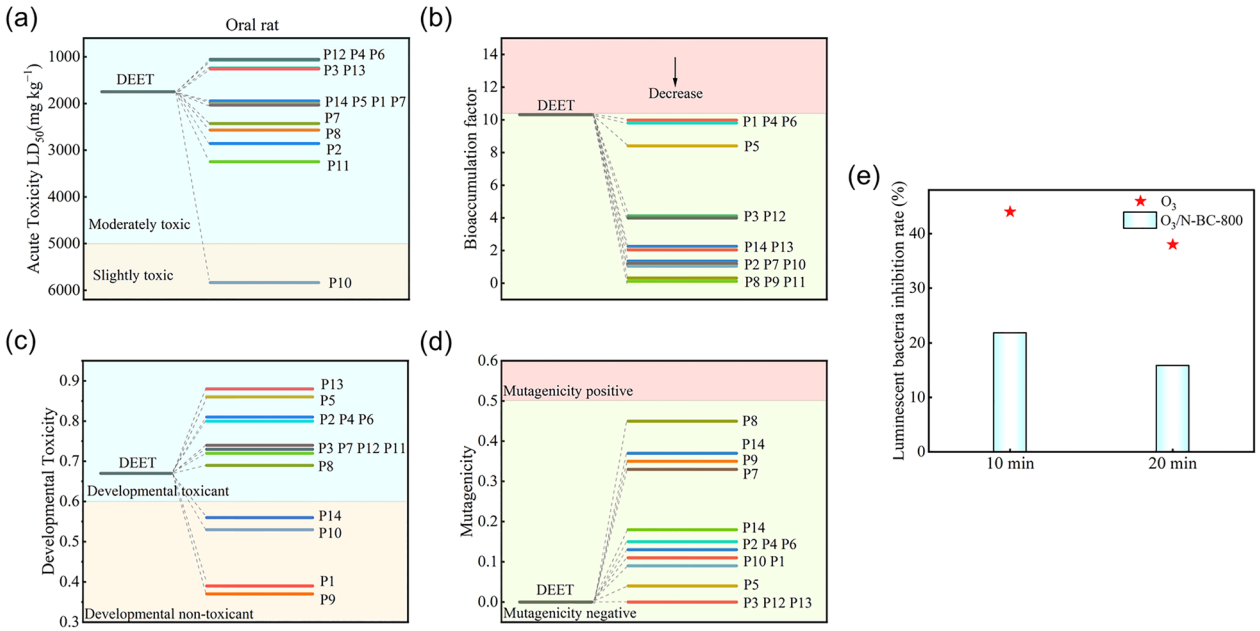

Fig. 11 **a** Acute toxicity, **b** bioaccumulation factor, **c** developmental toxicity, **d** mutagenicity, and **e** inhibition rate of Vibrio fischeri luminescence

4 Conclusions

This study successfully synthesized N-BC-800, which serves as an efficient catalyst for ozone-mediated degradation of the recalcitrant organic pollutant DEET. By regulating the surface morphology of the material, increasing its specific surface area, and introducing nitrogen-containing functional groups, its performance in ozone-catalyzed decomposition was significantly enhanced. Pyridinic N serves as the key active site, driving ozone activation and the generation of ROS. Experimental results demonstrate that the O_3/N-BC-800 system achieves a 94% removal rate for DEET, substantially exceeding that of undoped biochar. Mechanistic studies reveal that the catalytic reaction primarily proceeds via radical pathways involving $O_2^{\cdot-}$ and ·OH. Further investigations identified pyridinic N and surface C=O functional groups as key active sites. These sites promote efficient ozone decomposition and enhance ROS generation. Beyond its high-efficiency DEET degradation, N-BC-800 exhibited broad-spectrum catalytic activity toward various organic pollutants. It also effectively improved the biodegradability of real wastewater. This catalyst exhibits excellent structural stability and reusability. Even in the presence of competing components like natural organic matter and inorganic anions in real water bodies, the O_3/N-BC-800 system maintains outstanding pollutant degradation performance. Toxicity assessment results indicate that this treatment process significantly reduces the acute toxicity of effluent, demonstrating good environmental safety. In summary, nitrogen-doped biochar N-BC-800 exhibits outstanding ozone catalytic performance and broad environmental applicability, offering a promising sustainable technological solution for removing refractory organic pollutants from water bodies.

Supplementary Information

The online version contains supplementary material available at https://doi.org/10.1007/s42773-026-00607-x.

Additional file 1.

Author contributions

All authors contributed to the study conception and design. The first draft of the manuscript was written by Chaozhong Wang, and all authors commented on previous versions of the manuscript. All authors read and approved the final manuscript.

Funding

This work was supported by National Natural Science Foundation of China (No. 22206177).

Data availability

The datasets used or analyzed during the current study are available from the corresponding author upon reasonable request.

Declarations

Competing interests

All authors certify that they have no affiliations with or involvement in any organization or entity with any financial interest or non-financial interest in the subject matter or materials discussed in this manuscript.

Author details

[1]School of Environment and Chemical Engineering, Heilongjiang University of Science and Technology, Harbin 150022, China. [2]State Key Laboratory

of Environmental Criteria and Risk Assessment, Chinese Research Academy of Environmental Sciences, Beijing 100012, China. [3]Institute of Water Eco-Environment Research, Chinese Research Academy of Environmental Sciences, Beijing 100012, China.

Received: 7 November 2025 Revised: 23 February 2026 Accepted: 2 March 2026
Published online: 26 March 2026

References

Banhart F, Kotakoski J, Krasheninnikov AV (2010) Structural defects in graphene. ACS Nano 5:26–41. https://doi.org/10.1021/nn102598m

Cheng Y, Kang J, Yan P et al (2024) Surface oxygen vacancies prompted the formation of hydrated hydroxyl groups on ZnO in enhancing interfacial catalytic ozonation. Appl Catal B 341:123325. https://doi.org/10.1016/j.apcatb.2023.123325

Choi CH, Park SH, Woo SI (2012) Binary and ternary doping of nitrogen, boron, and phosphorus into carbon for enhancing electrochemical oxygen reduction activity. ACS Nano 6:7084–7091. https://doi.org/10.1021/nn3021234

Ding D, Yang S, Qian X et al (2020) Nitrogen-doping positively whilst sulfur-doping negatively affect the catalytic activity of biochar for the degradation of organic contaminant. Appl Catal B 263:118348. https://doi.org/10.1016/j.apcatb.2019.118348

Duan X, Sun H, Wang Y et al (2014) N-doping-induced nonradical reaction on single-walled carbon nanotubes for catalytic phenol oxidation. ACS Catal 5:553–559. https://doi.org/10.1021/cs5017613

Fotiou T, Triantis TM, Kaloudis T et al (2016) Assessment of the roles of reactive oxygen species in the UV and visible light photocatalytic degradation of cyanotoxins and water taste and odor compounds using C-TiO_2. Water Res 90:52–61. https://doi.org/10.1016/j.watres.2015.12.006

Fu Y, Yi Y, Wang Y et al (2025) A comprehensive review of modified biochar-based advanced oxidation processes for environmental pollution remediation: efficiency, mechanism, toxicity assessment. J Environ Manage 387:125872. https://doi.org/10.1016/j.jenvman.2025.125872

Gao X, Wang X, Li J et al (2020) Aquatic life criteria derivation and ecological risk assessment of DEET in China. Ecotoxicol Environ Saf 188:109881. https://doi.org/10.1016/j.ecoenv.2019.109881

He J, Long Y, Wang Y et al (2016) Aerosol-assisted self-assembly of reticulated N-doped carbonaceous submicron spheres for effective removal of hexavalent chromium. ACS Appl Mater Interfaces 8:16699–16707. https://doi.org/10.1021/acsami.6b04292

Jing Y, Jin W, Hong L et al (2022) Nitrogen-doped biochar as peroxymonosulfate activator to degrade 2,4-dichlorophenol: preparation, properties and structure–activity relationship. J Hazard Mater 424:127743. https://doi.org/10.1016/j.jhazmat.2021.127743

Kosak-Channing LF, Helz GR (1983) Solubility of ozone in aqueous solutions of 0–0.6 M ionic strength at 5–30.degree.C. Environ Sci Technol 17:145–149. https://doi.org/10.1021/es00109a005

Liu J-N, Chen Z, Wu Q-Y et al (2016) Ozone/graphene oxide catalytic oxidation: a novel method to degrade emerging organic contaminant N, N-diethyl-m-tolamide (DEET). Sci Rep 6:31405. https://doi.org/10.1038/srep31405

Ouyang D, Chen Y, Yan J et al (2019) Activation mechanism of peroxymonosulfate by biochar for catalytic degradation of 1,4-dioxane: important role of biochar defect structures. Chem Eng J 370:614–624. https://doi.org/10.1016/j.cej.2019.03.235

Restivo J, Orge CA, Guedes Gorito Dos Santos AS et al (2020) Nanostructured layers of mechanically processed multiwalled carbon nanotubes for catalytic ozonation of organic pollutants. ACS Appl Nano Mater 3:5271–5284. https://doi.org/10.1021/acsanm.0c00662

Song Z, Wang M, Wang Z et al (2019a) Insights into heteroatom-doped graphene for catalytic ozonation: active centers, reactive oxygen species evolution, and catalytic mechanism. Environ Sci Technol 53:5337–5348. https://doi.org/10.1021/acs.est.9b01361

Song Z, Zhang Y, Liu C et al (2019b) Insight into OH and $O_2^{\cdot-}$ formation in heterogeneous catalytic ozonation by delocalized electrons and surface oxygen-containing functional groups in layered-structure nanocarbons. Chem Eng J 357:655–666. https://doi.org/10.1016/j.cej.2018.09.182

Sui M, Sheng L, Lu K, Tian F (2010) FeOOH catalytic ozonation of oxalic acid and the effect of phosphate binding on its catalytic activity. Appl Catal B Environ 96:94–100. https://doi.org/10.1016/j.apcatb.2010.02.005

Sun Z, Zhao L, Liu C et al (2019) Catalytic ozonation of ketoprofen with in situ N-doped carbon: a novel synergetic mechanism of hydroxyl radical oxidation and an intra-electron-transfer nonradical reaction. Environ Sci Technol 53:10342–10351. https://doi.org/10.1021/acs.est.9b02745

Ta M, Zhang T, Wang T et al (2024) High-efficiency degradation of norfloxacin by Co-N Co-doped biochar synergistically activated peroxymonosulfate: experiments and DFT calculations. J Mater Chem A 12:17529–17543. https://doi.org/10.1039/D4TA02383H

Tian S-Q, Qi J-Y, Wang Y-P et al (2021) Heterogeneous catalytic ozonation of atrazine with Mn-loaded and Fe-loaded biochar. Water Res 193:116860. https://doi.org/10.1016/j.watres.2021.116860

Wan Z, Sun Y, Tsang DCW et al (2020) Customised fabrication of nitrogen-doped biochar for environmental and energy applications. Chem Eng J 401:126136. https://doi.org/10.1016/j.cej.2020.126136

Wang Y, Xie Y, Sun H et al (2016) Efficient catalytic ozonation over reduced graphene oxide for *p* -hydroxylbenzoic acid (PHBA) destruction: active site and mechanism. ACS Appl Mater Interfaces 8:9710–9720. https://doi.org/10.1021/acsami.6b01175

Wang Y, Cao H, Chen L et al (2018) Tailored synthesis of active reduced graphene oxides from waste graphite: structural defects and pollutant-dependent reactive radicals in aqueous organics decontamination. Appl Catal B Environ 229:71–80. https://doi.org/10.1016/j.apcatb.2018.02.010

Wang Y, Cao H, Chen C et al (2019a) Metal-free catalytic ozonation on surface-engineered graphene: microwave reduction and heteroatom doping. Chem Eng J 355:118–129. https://doi.org/10.1016/j.cej.2018.08.134

Wang Y, Chen L, Chen C et al (2019b) Occurrence of both hydroxyl radical and surface oxidation pathways in N-doped layered nanocarbons for aqueous catalytic ozonation. Appl Catal B Environ Energy 254:283–291. https://doi.org/10.1016/j.apcatb.2019.05.008

Wang L, Xu H, Jiang N et al (2020a) Trace cupric species triggered decomposition of peroxymonosulfate and degradation of organic pollutants: Cu(III) being the primary and selective intermediate oxidant. Environ Sci Technol 54:4686–4694. https://doi.org/10.1021/acs.est.0c00284

Wang Y, Duan X, Xie Y et al (2020b) Nanocarbon-based catalytic ozonation for aqueous oxidation: engineering defects for active sites and tunable reaction pathways. ACS Catal 10:13383–13414. https://doi.org/10.1021/acscatal.0c04232

Wang S, Li T, Cheng X et al (2023a) Regulating the concentration of dissolved oxygen to achieve the directional transformation of reactive oxygen species: a controllable oxidation process for ciprofloxacin degradation by calcined CuCoFe-LDH. Water Res 233:119744. https://doi.org/10.1016/j.watres.2023.119744

Wang Y, Lin Y, Yang C et al (2023b) Calcination temperature regulates non-radical pathways of peroxymonosulfate activation via carbon catalysts doped by iron and nitrogen. Chem Eng J 451:138468. https://doi.org/10.1016/j.cej.2022.138468

Wei K, Wang Z, Ouyang C et al (2020) A hybrid fluidized-bed reactor (HFBR) based on arrayed ceramic membranes (ACMs) coupled with powdered activated carbon (PAC) for efficient catalytic ozonation: a comprehensive study on a pilot scale. Water Res 173:115536. https://doi.org/10.1016/j.watres.2020.115536

Xiao J, Rabeah J, Yang J et al (2017) Fast electron transfer and •OH formation: key features for high activity in visible-light-driven ozonation with C3N4 catalysts. ACS Catal 7:6198–6206. https://doi.org/10.1021/acscatal.7b02180

Xiong S, Tang M, Jiang W et al (2023) PCDD/F adsorption enhancement over nitrogen-doped biochar: A DFT-D study. J Environ Manage 344:118611. https://doi.org/10.1016/j.jenvman.2023.118611

Xu B, Qi F, Zhang J et al (2016a) Cobalt modified red mud catalytic ozonation for the degradation of bezafibrate in water: Catalyst surface properties characterization and reaction mechanism. Chem Eng J 284:942–952. https://doi.org/10.1016/j.cej.2015.09.032

Xu Y, Mo Y, Tian J et al (2016b) The synergistic effect of graphitic N and pyrrolic N for the enhanced photocatalytic performance of nitrogen-doped graphene/TiO_2 nanocomposites. Appl Catal B Environ 181:810–817. https://doi.org/10.1016/j.apcatb.2015.08.049

Xu L, Wu C, Liu P et al (2020) Peroxymonosulfate activation by nitrogen-doped biochar from sawdust for the efficient degradation of organic pollutants. Chem Eng J 387:124065. https://doi.org/10.1016/j.cej.2020.124065
Xu A, Fan S, Meng T et al (2022) Catalytic ozonation with biogenic fe-mn-co oxides: Biosynthesis protocol and catalytic performance. Appl Catal B Environ 318:121833. https://doi.org/10.1016/j.apcatb.2022.121833
Yang W, Wu T (2022) Evaluation of plasmon-enhanced catalytic ozonation for the abatement of micropollutants in environmental matrices. Water Res 211:118072. https://doi.org/10.1016/j.watres.2022.118072
Yang Y, Jiang J, Lu X et al (2015) Production of sulfate radical and hydroxyl radical by reaction of ozone with peroxymonosulfate: A novel advanced oxidation process. Environ Sci Technol 49:7330–7339
Yu G, Wang Y, Cao H et al (2020) Reactive oxygen species and catalytic active sites in heterogeneous catalytic ozonation for water purification. Environ Sci Technol. https://doi.org/10.1021/acs.est.0c00575
Zeng S, Xia X, Miao S et al (2024) Green synthesis of highly pyrrolic nitrogen-doped biochar for enhanced tetracycline degradation: New insights from endogenous mineral components and organic nitrogen synergy. J Clean Prod 444:141177. https://doi.org/10.1016/j.jclepro.2024.141177
Zhang S, Gitungo S, Dyksen JE et al (2021) Indicator compounds representative of contaminants of emerging concern (CECs) found in the water cycle in the United States. Int J Environ Res Public Health 18:1288. https://doi.org/10.3390/ijerph18031288
Zhao Y, Yu L, Song C et al (2022) Selective degradation of electron-rich organic pollutants induced by CuO@biochar: the key role of outer-sphere interaction and singlet oxygen. Environ Sci Technol 56:10710–10720. https://doi.org/10.1021/acs.est.2c01759
Zhou C, Zhou P, Sun M et al (2022) Nitrogen-doped carbon nanotubes enhanced Fenton chemistry: role of near-free iron(III) for sustainable iron(III)/iron(II) cycles. Water Res 210:117984. https://doi.org/10.1016/j.watres.2021.117984
Zhou T, Zhu S, Li X et al (2025) Unraveling the synergistic mechanism of urea and sodium carbonate during biochar modification and peroxymonosulfate activation for wastewater decontamination. Biochar 7:35. https://doi.org/10.1007/s42773-025-00433-7
Zhu H, Guo A, Wang S et al (2022) Efficient tetracycline degradation via peroxymonosulfate activation by magnetic Co/N Co-doped biochar: emphasizing the important role of biochar graphitization. Chem Eng J 450:138428. https://doi.org/10.1016/j.cej.2022.138428